Journal of Fluids and Structures 123 (2023) 104000

Contents lists available at ScienceDirect

Journal of Fluids and Structures

journal homepage: www.elsevier.com/locate/jfs

The roles of fish median fins on the hydrodynamics and muscle actuation in *carangiform* swimming

Yuhan Li [a], Jialei Song [a,b,*], Yong Zhong [c,*], Bo Yin [d]

[a] Guangdong Provincial Key Laboratory of Intelligent Disaster Prevention and Emergency Technology, Dongguan University of Technology, Dongguan, China
[b] School of Mechanical Engineering, Dongguan University of Technology, Dongguan, China
[c] Shien-Ming Wu School of Intelligent Engineering, South China University of Technology, Guangzhou, China
[d] Institute of Mechanics, Chinese Academy of Sciences, Beijing 100190, China

ARTICLE INFO

Keywords:
Median fins
Muscle actuation
Hydrodynamics
Numerical simulation

ABSTRACT

Compared with swimmers with only caudal fins, swimmers with additional median fins, i.e. dorsal and anal fins can improve fish locomotive performance in cruising swimming. However, the effects of these fins on hydrodynamics, particularly on muscle actuation, remain poorly understood. In this study, we investigated four models (model i: with dorsal and anal fins; ii: without dorsal and anal fins; iii: with dorsal fin and without anal fin; iv: without dorsal fin and with anal fin) of cruising crucian carp using three-dimensional computational fluid dynamics (CFD) modeling. This study shows that both speed and thrust are improved in the presence of dorsal and anal fins, as the wake shed from these fins is intercepted by the caudal fin. Dorsal fin is discovered to increase the swimming efficiency, internal torque and the speed of the torque wave, whereas anal fin decreases these parameters. The adverse effects of these two fins are due to the difference in the phase of the forces generated on them and consequently affect the muscle actuation in the midbody and energy transmission around the peduncle. Our results provide new insight into the roles of the median fins in swimming performance and muscle actuation, which might benefit the design of fish-like robots.

1. Introduction

Fish undulate their body and fins to gain thrust from the interaction with surrounding fluid by generating a backward wave in cruising swimming. In this process, the contraction of muscles on the lateral sides of fish provides power. A clear understanding of muscular actuation is of importance to elucidate fish propulsion, to understand ecological behavior from a biologist's perspective and to optimize the active actuation of fish-like robots from an engineer's perspective.

Experimentally, researchers have used electromyography (EMG) to directly measure muscle activation in different fish species, including lamprey, trout, mackerel, saithe, eel, carp and scup (Gillis, 1998; Rome et al., 1993; Van Leeuwen et al., 1990; Wardle and Videler, 1993; Williams et al., 1989), as the stimulation of EMG indicates muscle activation. For fish with different body forms and swimming patterns, the muscle activation patterns are significantly different. In general, the EMG speed is lower in *anguilliform* swimmers than in *carangiform* swimmers (Wardle et al., 1995). In addition, for *anguilliform* swimmers, such as lampreys, the EMG

* Corresponding authors.
E-mail addresses: songjl@dgut.edu.cn (J. Song), zhongyong@scut.edu.cn (Y. Zhong).

https://doi.org/10.1016/j.jfluidstructs.2023.104000
Received 7 April 2023; Received in revised form 20 September 2023; Accepted 2 October 2023
Available online 21 October 2023

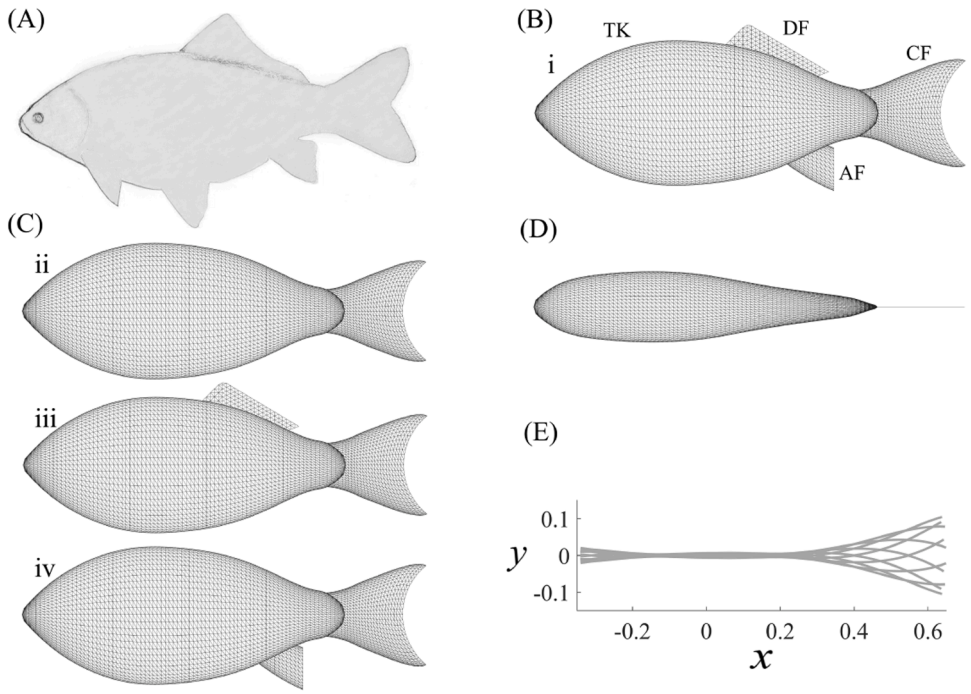

Fig. 1. The geometrical models and the variation of middle lines. (A) Fish prototype, (B) side view of the simplified mode (i), (C) side view of the simplified model without dorsal and anal fins (ii), with dorsal fins only (iii) and with anal fins only (iv), (D) top view of the simplified model, (E) the selected snapshot of the middle lines.

duration and the phase relationship between muscle strain cycles and EMG activity vary little along the body posterior. Meanwhile, for *carangiform* swimmers, such as carps and mackerels, a significant variation in EMG duration and the EMG/strain phase relationship along the body is observed (Van Leeuwen et al., 1990; Wardle and Videler, 1993; Williams et al., 1989). The comparison of EMG signals and body undulation in cruising swimming shows an interesting phenomenon, that is, the EMG wave that represents muscle activation travels posterior at a speed higher than that of the body curvature wave, which has been termed "neuromechanical phase lag" (NPL) (Ding et al., 2013). As the muscle activation pattern varies with species, such NPL combined with EMG stimulation, contraction kinematics information reflects the muscle power output along the fish body (Altringham and Ellerby, 1999).

Theoretically, researchers previously predicted muscle activation and power output using oversimplified models such as resistive force theory and elongated body theory, and such theoretical analyses confirmed NPL (Chen et al., 2011; Hess and Videler, 1984). In addition, it was also revealed that the energy from swimming was supplied primarily by the mid-body muscle, transmitted through the body in the form of elastic energy (Hess and Videler, 1984). In a study of the lamprey, Tytell et al. revealed that body stiffness could affect the NPL using the unvaried muscle activation pattern (Tytell et al., 2010). McMillen et al. constructed an *anguilliform* model to investigate the causes of neuromechanical phase lag, concluding that NPL derives from several factors, including passive viscoelasticity, geometric properties of the body and active muscle properties. In particular, taking the hydrodynamic force off causes the torque wave speed to decrease midbody and increase toward the tail (McMillen et al., 2008). However, the hydrodynamic forces in these previous models cannot be accurately predicted, as they relied on strong assumptions or oversimplification. The small amplitude assumption used for hydrodynamics prediction for fish undulation limited the reliable implementation on the real fish tail beats, which usually have an amplitude of 0.2 body length (Hess and Videler, 1984). Meanwhile, the fish model usually uses a slender body or thin plate geometrically, making accurate inertial torque analysis impossible. To eliminate the limitations of these modeling methodologies, Ming et al. used a 3D CFD simulation with a self-propelled fish model to investigate the torque and power output patterns for *anguilliform* and *carangiform* swimmers (Ming et al., 2019). They analyze the energy transfer, storage and release within the body, explaining the mechanisms of muscle activation regarding fluid/inertial torque and body elasticity. The geometry of their models used sole truck and tail, which captures the main structure of fish, but did not include median fins, such as dorsal and anal fins.

A hallmark of fish swimming is the coordination between body undulation and the motion of the median fins, such as the dorsal, anal and caudal fins (Lauder and Drucker, 2004; Sfakiotakis et al., 1999). Hydrodynamically, the dorsal and anal fins have been regarded as passive surfaces that stabilize swimming during cruising swimming (Lauder and Drucker, 2004). Meanwhile, dorsal and anal fins were discovered to be used to increase speed and efficiency. As the vortex shed by the dorsal and anal fins is intercepted by the caudal fin, the propulsive performance of the caudal fin might be enhanced, allowing the fish to achieve faster speeds or higher efficiency (Lighthill, 1970; Weihs, 1989). Consequently, the presence of dorsal and anal fins might affect muscle activation patterns, and this needs further study.

In this paper, we reconstruct a three-dimensional model of a crucian carp with dorsal and anal fins and simulated the swimming

Table 1
Parameters of the simplified model.

Parameter	Value
Mass, M	0.0192
Width, 2b	0.1660
Height, 2a	0.3406
Area of caudal fin, S_c	0.0382
Area of dorsal fin, S_d	0.0164
Area of anal fin, S_a	0.0108

process of the swimmer using self-propelled 3D CFD simulation. By comparing the swimming parameters of swimmers with/without dorsal and anal fins, we aim to explain how dorsal and anal fins influence swimming performance in terms of muscle activation patterns.

2. Materials and methods

2.1. Geometrical modeling and kinematics

We used a crucian carp as the prototype for the fish model in our modeling (Fig. 1A). The surface of the fish was reconstructed with triangular grids using the surface data by 3D scanning (ZGSCan 717, Guangdong, China). To avoid divergence during CFD simulations, the reconstructed shape was made without sharp and small protrusions, and the fish was interpolated using three splines to ensure a smooth surface. The body trunk (TK), caudal fin (CF), dorsal fin (DF) and anal fin (AF) of the carp were retained in the reconstructed model to investigate their contribution during swimming. For ease of description, we use "model i", "model ii", "model iii" and "model iv" to describe our models with/without different median fins (Fig. 1B and C). All fins are zero-thickness membrane structures, and the fish body trunk is a three-dimensional block, and the top view is shown in Fig. 1D. The entire fish has 11,906 elements, including 9600 elements for the body trunk, 1560 for the caudal fin, 330 for the dorsal fin and 416 for the anal fin. The length of the fish model is set as $L = 1$, the density is the same as water, $\rho = 1$, and the parameters of the model are shown in Table 1.

The kinematics for undulatory locomotion are in the *carangiform* form, with a posteriorly traveling wave with the largest wave amplitude at the tail (Zha et al., 2019). In this paper, the centerline curvature $\kappa(s,t) = A(s)\sin(ks - \omega_u t)$ is used to describe the deformation of the body of the fish, where s is the arc distance along the axis from the apex of the fish head, $k = 2\pi/\lambda$ is the wavenumber defined by the wavelength of the body λ=1, and ω_u is the angular frequency. We use the undulation period $T = 2\pi/\omega_u$=1. $A(s)$ is the amplitude envelope of the curvature, which is $A(s) = a_0 + a_1 s + a_2 s^2$, where the parameters were set to $a_0 = 1$, $a_1 = -3.2$ and $a_2 = 5.6$ based on the experimental results to match the envelope of the real fish movements (Hess and Videler, 1984). Please note that the horizontal axis refers to x is different from s. With the curvature above, the position of a body segment relative to the head $r_h = (x_h, y_h)$ can be computed by integrating the curvature twice:

$$\begin{aligned} \theta(s,t) &= \int_0^s \kappa(l,t)dl \\ x_h(s,t) &= \int_0^s \cos(\theta(l,t))dl \\ y_h(s,t) &= \int_0^s \sin(\theta(l,t))dl \end{aligned} \tag{1}$$

To ensure the conservation of the linear momentum of the fish before hydrodynamic force is applied, the center of mass (COM) is computed, and the origin of the coordinates is moved to the COM, that is, $(x', y') = (x_h - x_{COM}, y_h - y_{COM})$. Next, we assume that there is an angular velocity $\omega_b(t)$about the COM and compute the variation in angular momentum$L_t(t)$. Angular momentum conservation requires $dL_t/dt = 0$, then the angular velocity $\omega_b(t)$ can be computed. The angle of rotation of the body is obtained by $\theta_b = \int \omega_b \mathrm{d}t$. Every point on the body at a time instant t is rotated by $\theta_b(t)$ so that the angular momentum is conserved (Ming et al., 2019). According to the above method, we obtained the middle lines of the fish model for kinematic specification, which are shown in Fig. 1E. In the fish model, the motion of the dorsal and anal fins is specified using the same curvature of the middle lines of the body.

2.2. Numerical methods and simulation setup

In this paper, the fluid dynamics of a three-dimensional incompressible, unsteady, viscous fluid around a swimmer are solved using a fluid solver based on the intrusive boundary method. The fluid solver is able to simulate the motion of complex embedded objects, including zero-thickness membranes and three-dimensional solids, and has been successfully applied to the swimming of fish (Song et al., 2021, 2018; Zhong et al., 2022) and the flight of birds (Song et al., 2014, 2016). The governing equations for the fluid around the swimmer are assumed to be as follows:

$$\nabla \cdot \boldsymbol{u} = 0 \tag{2}$$

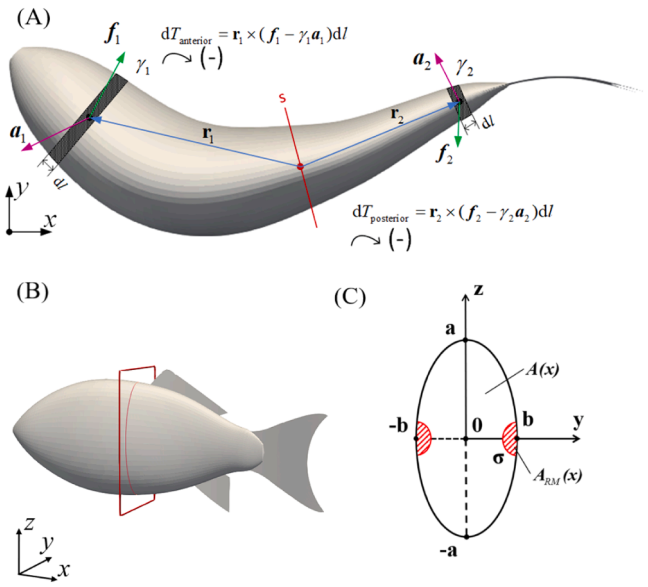

Fig. 2. Diagram of internal torque and stress distribution. (A) The black shaded areas represent the element length along the body axis, γ is its linear density along the fish middle line, $\boldsymbol{a}$ is the acceleration of the body segment and $\mathbf{r}$ is the displacement from the transection of interest. (B) The transection of interest to calculate torque. (C) Simplified distribution of red muscle on the section of interest.

$$\frac{\partial \boldsymbol{u}}{\partial t} + (\boldsymbol{u} \cdot \nabla)\boldsymbol{u} = -\frac{1}{\rho}\nabla p + \upsilon \Delta \boldsymbol{u} \tag{3}$$

where u denotes the velocity vector, p denotes the pressure, and$\rho$and $\upsilon$are the density and kinematic viscosity of water, respectively. In this study, the fluid-body interaction is included by implementing the loose coupling (LC-FSI) explicit projection method (Borazjani and Sotiropoulos, 2010). The translational motion of swimmer's center of mass is obtained by solving the equation of Newton's second law of motion:

$$M\frac{d\boldsymbol{U}}{dt} = \boldsymbol{F} \tag{4}$$

$$\frac{d\boldsymbol{r}}{dt} = \boldsymbol{U} \tag{5}$$

where $M = 0.0192$ is the mass of the swimmer, $\mathbf{U}$ is the velocity vector of the COM, $\mathbf{F}$ is the integrative force vector and $\mathbf{r}$ is the displacement of COM of the swimmer. Because the bodies of the swimmers are deforming, the governing equation for the angular degree of freedom is $d(I\omega)/dt = T_{tot}$, where I is the moment of inertia, ω is the angular velocity of the body, and T_{tot} is the total torque computed by integrating the contributions from the hydrodynamic forces on the surface of the swimmer. As the fish model deforms throughout the entire cycle and the kinematics is prescribed, the values of I and $\dot{I}$ of each position are determined, with I ranging from 4.959×10^{-4} to 4.965×10^{-4}. The angular velocity of the whole fish ω can be obtained by numerically solving equation $\dot{\omega} = (T_{tot} - \dot{I}\omega)/I$, and subsequently the angle is obtained. The detailed algorithm of in-house CFD code is described in reference (Song et al., 2021).

The entire flow field was discretized with a nonuniform Cartesian grid with dimensions of $8 \times 5.1 \times 5$ in the x, y and z directions, using a total of $411 \times 201 \times 181 \approx 15$ million grid points (**Fig. S1** in supplementary materials). The grid was locally refined around the fish with a minimum spacing of $0.005 \times 0.005 \times 0.005$ as the mesh convergence study was performed and is shown in the supplementary materials (**Table S1, Figs. S2** and **S3**). The region of refined grid is $1.6 \times 0.7 \times 0.6$. An incoming flow with speed Uo is established at the inlet to stop the swimmer from leaving the refined grid zone (see **Fig. S1** in the supplementary materials).

With the exception of the dorsal and anal fins, the entire fish model is symmetrical about the x-y plane, with the body centerline in the middle plane, so that the displacement and deflection motion of the fish in the z direction is ignored. In fact, the average force applied to the fish in the z-direction is less than 1/20 of that applied in the plane of motion. At inlet, an incoming velocity $U_o = 0.3$ L/T is set to avoid the flow field to be too large as the fish swims through the water. The Reynolds number is defined as$Re = U_s L/\nu_k$, where U_s is the free swimming speed in static fluid, which equals U_o plus the swimming speed in simulation, and $\nu_k = 1/15{,}000$ is the kinematic viscosity to make $Re = 4680$.

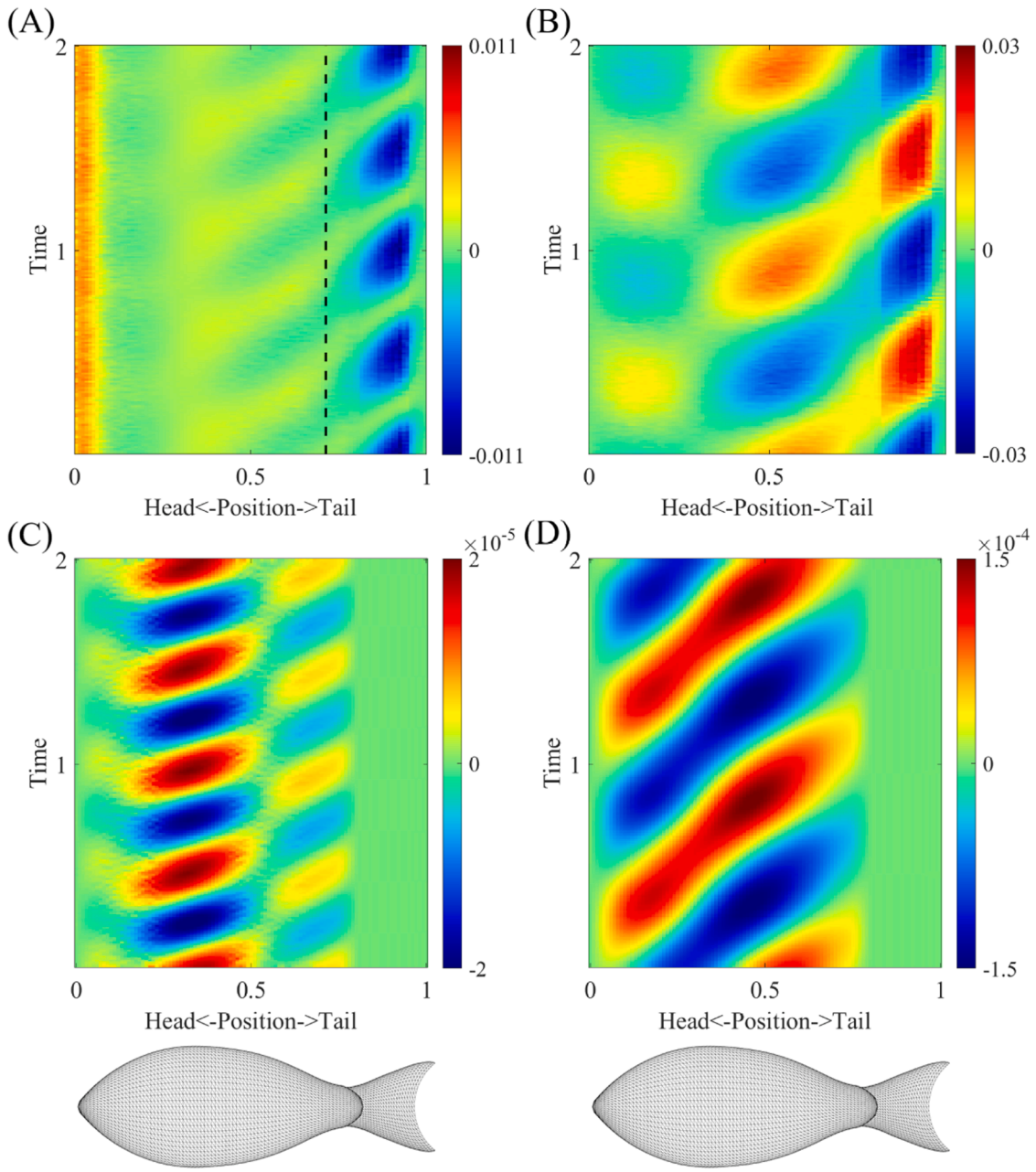

Fig. 3. Spatiotemporal distribution of the hydrodynamic force (A and B) and inertial force (C and D) in the x (A and C) and y (B and D) directions in two periods for model ii.

2.3. Force, internal torque, and muscle stress

The force components of the entire fish model are normalized by the fluid density ρ , the maximum frontal cross-section area A_m, and the average speed of swimming $\overline{V_x}$. Thus, we obtain the normalized force as

$$C_x = \frac{F_x}{0.5\rho\overline{V_x}^2 A_m}, C_y = \frac{F_y}{0.5\rho\overline{V_x}^2 A_m}, C_z = \frac{F_z}{0.5\rho\overline{V_x}^2 A_m} \tag{6}$$

where F_x, F_y, and F_z are the force components in the x, y and z directions, respectively.

With the data produced by CFD simulations, we calculate the spatiotemporal distribution of the hydrodynamic force along the fish body $\boldsymbol{f}$, e.g. the force per unit arc length along the midline. The inertial force per unit length on the fish body is calculated as follows:

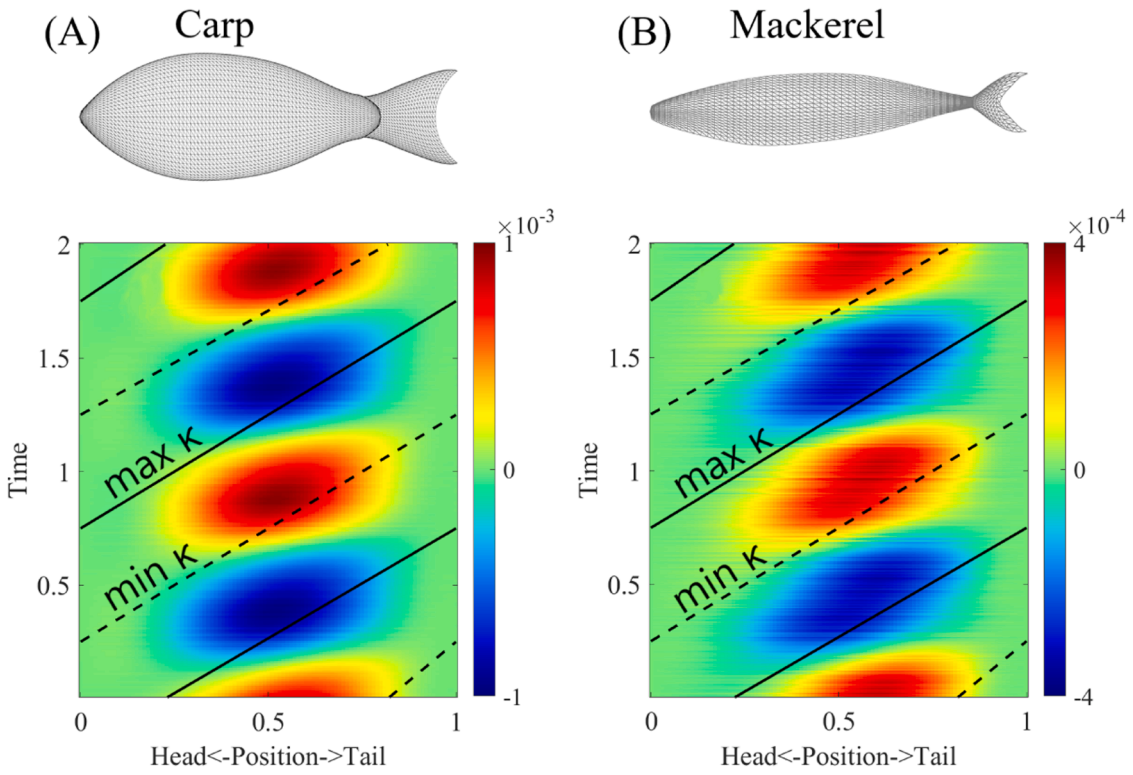

Fig. 4. Spatiotemporal distribution of the internal torque in two periods for model ii (A) and mackerel (B). The solid and dashed lines indicate the maximum and minimum curvatures, respectively.

take a small segment along the middle line with arc length dl, and treat it as being rigid, and the inertial force according to d'Alembert's principle is $-\rho_0 \boldsymbol{A} d l \boldsymbol{a}$, where ρ_0 is the density of fish body (same to the density of fluid), $\boldsymbol{A}$ is the cross-section area, and $\boldsymbol{a}$ is the acceleration of the COM of segment dl (Fig. 2). Therefore, the inertial force distribution per unit arc length is $-\rho_0 \boldsymbol{A}\boldsymbol{a}$ or $-\gamma \boldsymbol{a}$ as $\gamma=\rho_0 \boldsymbol{A}$ is the line density. The internal torque, or the torque exerted by the muscle on the transection of the body, is calculated including both the hydrodynamic and the body inertial effect. The internal torque can be calculated by integrating from the tail forward (Eq. (7a)) or from the head backward (Eq. (7b)),

$$T_{posterior}(s,t) = -\boldsymbol{e}_z \cdot \int_s^1 \boldsymbol{r} \times (\boldsymbol{f} - \gamma \boldsymbol{a}) dl \tag{7a}$$

$$T_{anterior}(s,t) = \boldsymbol{e}_z \cdot \int_0^s \boldsymbol{r} \times (\boldsymbol{f} - \gamma \boldsymbol{a}) dl \tag{7b}$$

Theoretically, $T = T_{posterior} = T_{anterior}$, and the relative error becomes apparent at the ends where the torques are smaller (**Fig. S4** in the supplementary materials). To reduce the error of the torque, the weighted average is used in the following formula:

$$T = sT_{\text{posterior}} + (1+s)\text{T}_{\text{anterior}} \tag{8}$$

It should be noted that Eq. (8) may provide different result from that predicted by fluid-structure interaction (Godoy-Diana and Thiria, 2018). Nevertheless, we believe it can provide the general pattern of muscle actuation, and also the effect of dorsal and anal fins on muscle actuation in a much simpler way. In addition, the prescribed curvature model offers a straightforward path to estimate the resultant actuation with observed behavior of fish and fish-like robot. According to previous observations, fish use red muscles or slow muscles to power cruising steady swimming (Rome et al., 1993; Syme, 2005; Videler, 1993). The red muscles are distributed on the lateral end of the transection, which is shown in Fig. 2C. In most fish, the red muscle accounts for less than 10 % of the muscle tissue, but the proportion increases near the tail end (Syme, 2005), so we represent the red muscle region as two semielliptical regions symmetrically distributed on both sides with an area of 10 % of the cross-sectional area, as shown in Fig. 2C. Thus, the stress values σ in the red muscle region can be calculated as

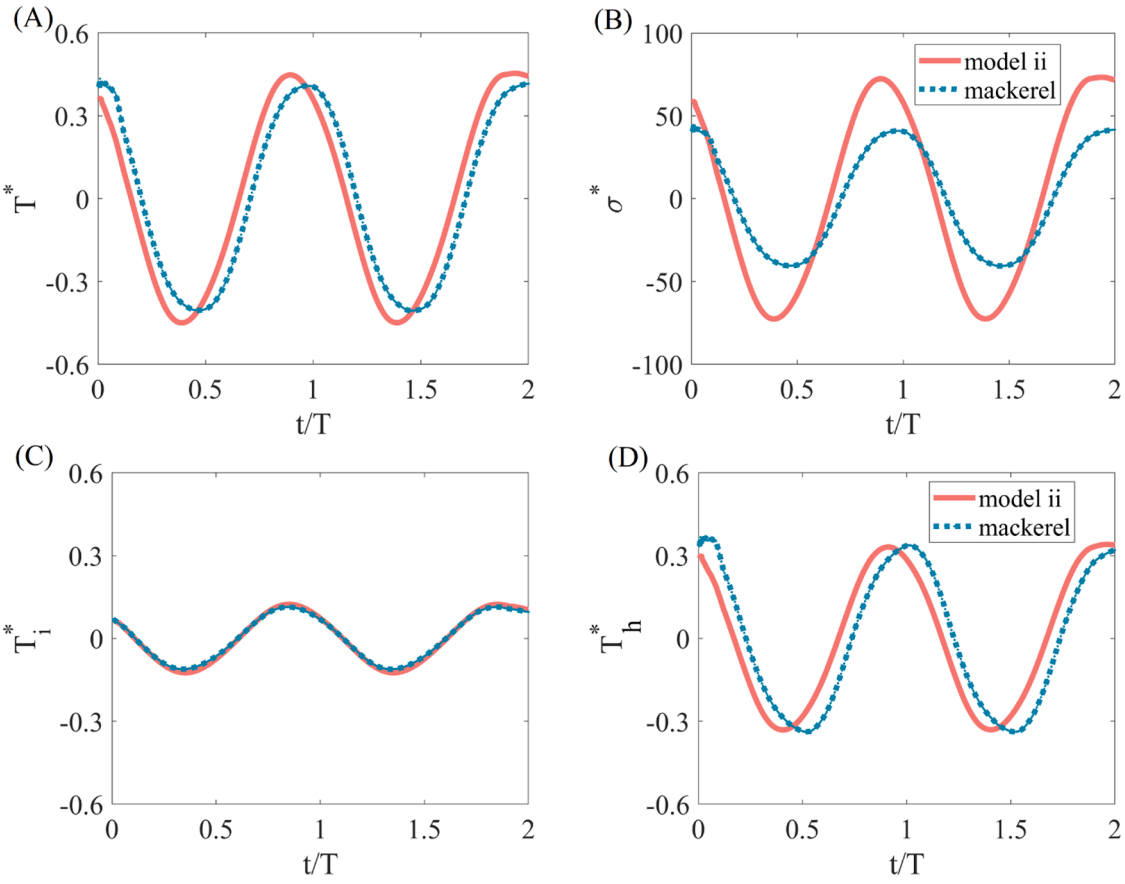

Fig. 5. The variation in dimensionless torque and stress at the position of maximum torque in two periods for "model ii" and mackerel. (A) The variation in dimensionless internal torque, (B) the variation in dimensionless stress, (C) the variation in dimensionless inertial torque and (D) the variation in dimensionless hydrodynamic torque.

$$\sigma = \frac{F_{muscle}}{A_{rm}} = \frac{2T/b}{0.5 * \frac{1}{10}\pi ab} = \frac{40}{ab^2\pi}T \tag{9}$$

where $F_{muscle}$is the muscle force and A_{rm} is the area of red muscle on concave side, a and b are the long and short semi-axes of the ellipse section of interest. The non-dimensional stress and torque are as follows:

$$\sigma^* = \frac{\sigma}{0.5\rho\overline{V_x}^2}, T^* = \frac{T}{0.5\rho\overline{V_x}^2 A_m L} \tag{10}$$

2.4. Efficiency

Previous studies have shown that the dorsal and anal fins could improve the swimming efficiency when compared with the model without these fins at the same swimming speed (Han et al., 2020). In this study, we compare the efficiency at its final steady cruising states. Two approaches to evaluate the efficiency, *quasi-propulsive efficiency* η_q and efficiency on the caudal fin merely η_c, are adopted, similar to previous work(Song et al., 2021; Zhong et al., 2022). The *quasi-propulsive efficiency* refers to the overall Froude efficiency of the integrated model but with different definitions of thrust. The formula to calculate *quasi-propulsive efficiency* η_q is given by equation:

$$\eta_q = \frac{D_0\overline{V_x}}{P_{in}} \tag{11}$$

where $P_{\text{in}} = \int_S \boldsymbol{f} \cdot \boldsymbol{v} dS$ denotes the hydrodynamic power consumed on the entire fish, $\overline{V_x}$is the average forward velocity at steady state, and D_0 denotes the drag towing the swimmer in a rigid-straight condition at constant speed $\overline{V_x}$, which is obtained by towing each of the four models at the corresponding average speed. The caudal fin efficiency $\eta_c$is defined as the ratio of the thrust coefficient of tail $C_{Tt,tail}$to the corresponding power coefficient $C_{P,tail}$,

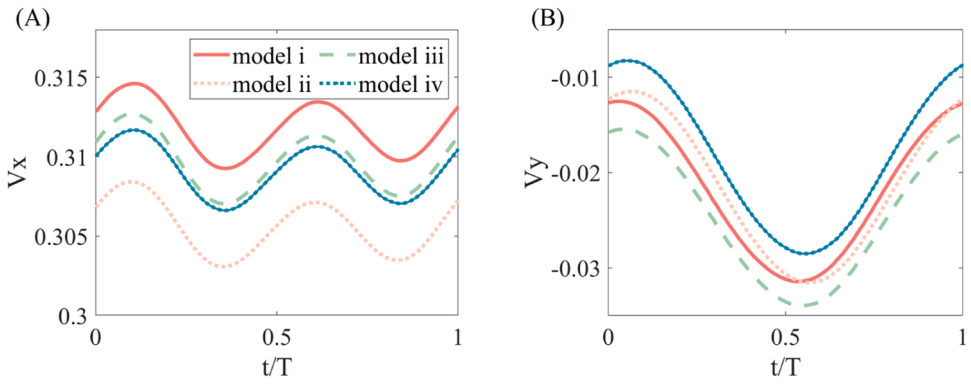

Fig. 6. The velocity variation in the x(A) and y(B) directions in the 20th period of four models.

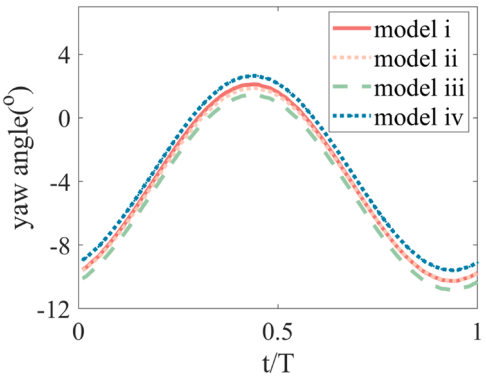

Fig. 7. The yaw angle variation in the 20th period of four models.

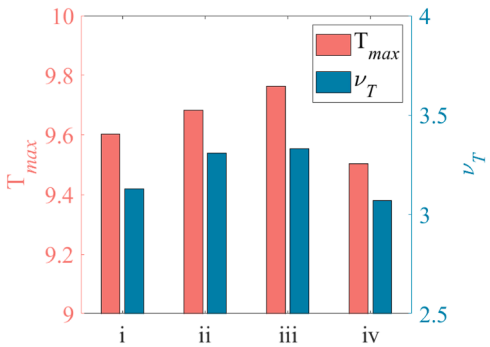

Fig. 8. The maximum internal torques and the speeds of the torque wave moving backward for model i, model ii, model iii and model iv.

$$\eta_c = \frac{Tt\overline{V_x}}{P_{in,tail}} = \frac{C_{Tt,tail}}{C_{P,tail}} \tag{12}$$

where $C_{P,tail} = \int_{S,tail} \boldsymbol{f}\cdot\boldsymbol{v}dS/(0.5\rho\overline{V_x}^3 S)$, $C_{Tt,tail} = Tt\overline{V_x}/(0.5\rho\overline{V_x}^3 S)$, and Tt is the thrust on tail.

3. Results

To achieve a relatively steady state where the average forward velocity does not change, we simulate 20 movement cycles, and the data used in the following are from the last two cycles unless otherwise stated (**Fig. S5** in the supplementary material). The final free swimming speed of model i is 0.312 ± 0.003 in nondimensionalized units. The corresponding Strouhal number is 0.57, which is close

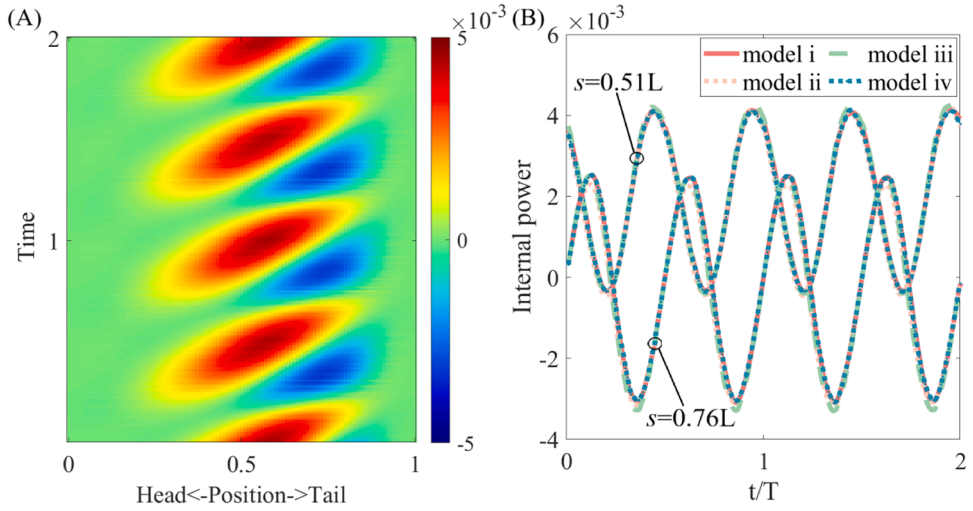

Fig. 9. Spatiotemporal distribution of the internal power of model ii (A) and time course at the positions of 0.51 L and 0.76 L in two periods for four models (B).

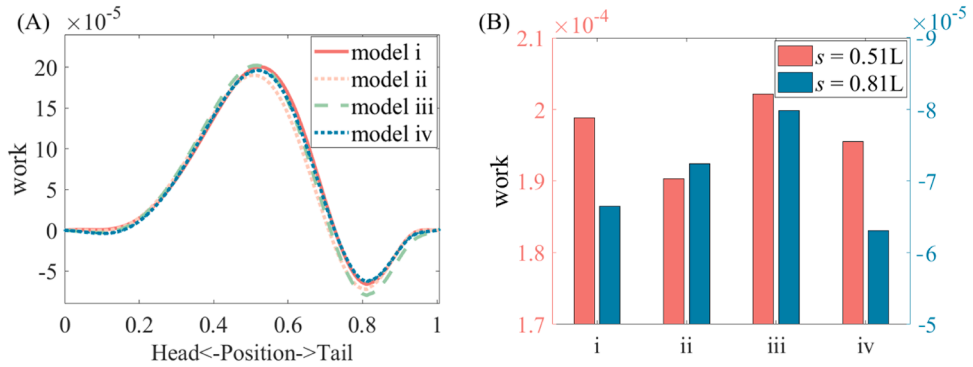

Fig. 10. The work done over a cycle by muscles along the bodies of four Models (A) and the work done at 0.51 L and 0.81 L (B).

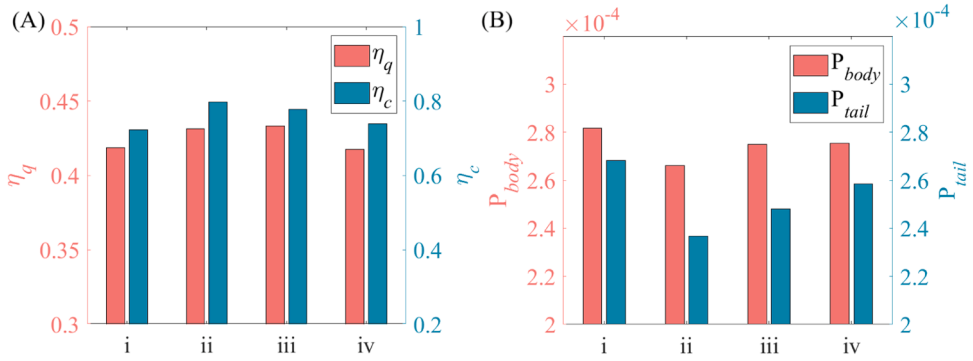

Fig. 11. The efficiency(A) and power consumed on the body and tail(B) for model i, model ii, model iii and model iv.

to that in previous numerical studies ($St = 0.61$) of mackerel fish at $Re = 4000$ (Borazjani and Sotiropoulos, 2010).

3.1. Investigating model ii

First, we adopt the model without dorsal and anal fins (model ii) as a benchmark to study the dynamics of the trunk and caudal fin only. In terms of the hydrodynamic force, its distribution over time in model ii is shown in Fig. 3A and B, with A presenting the force in

Table 2
Kinematic and dynamic parameters of four cruising swimmers.

	$\overline{V_x}$	$D_0(\times 10^{-4})$	$C_{Tt,tail}$	$C_{P,tail}$	η_q	η_c
model i	0.312	−7.52	0.290	0.402	0.419	0.722
model ii	0.306	−7.08	0.300	0.377	0.431	0.798
model iii	0.310	−7.37	0.295	0.380	0.433	0.778
model iv	0.309	−7.27	0.294	0.398	0.418	0.738

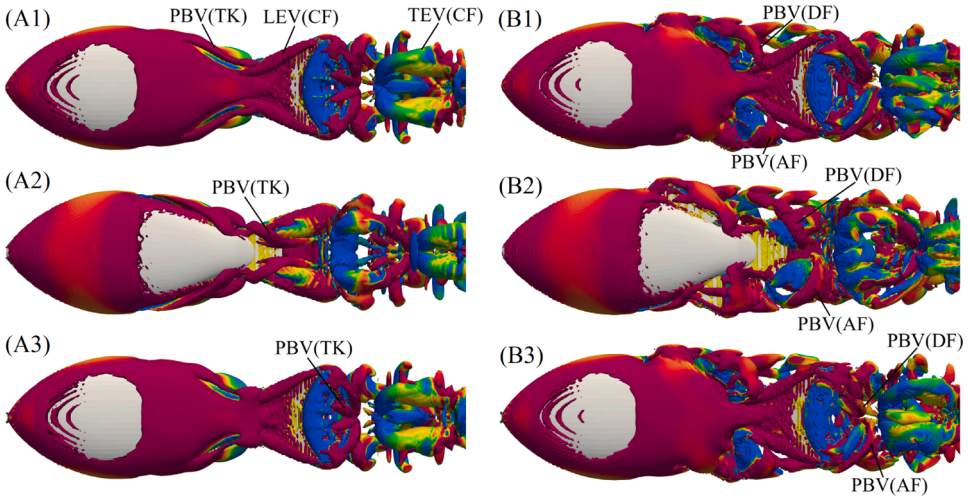

Fig. 12. Development and variation of the vortex 3D structure for model ii (left column) and model i (right column). (A1,B1) at $t/T = 0$, (A2,B2) at $t/T = 0.5$ and (A3,B3) at $t/T = 1$.

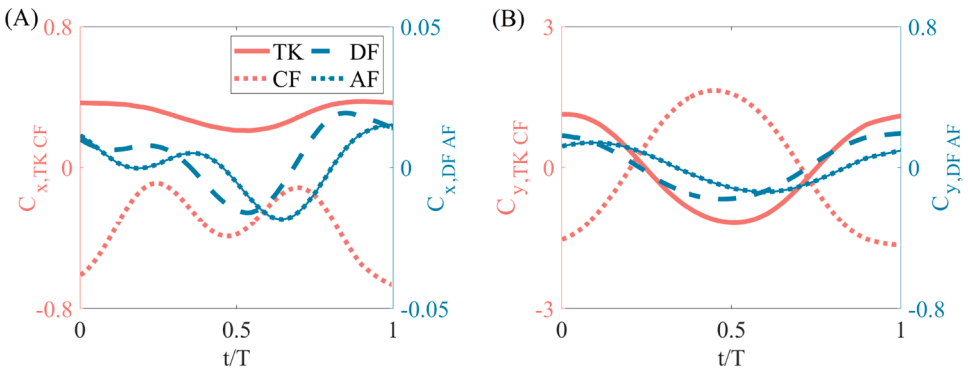

Fig. 13. The force coefficient variation in the x(A) and y(B) directions in the 20th period of model i.

the *x* direction and B presenting the lateral force. Force in the *x* direction shows that thrust is primarily generated on the caudal fin, while drag is introduced at the anterior body. The critical location is 0.71 L from the head, where the periodically average thrust/drag is zero (Fig. 3A). Meanwhile, the lateral force along the entire body varies periodically with the direction switch, making the periodically average lateral force zero. The maximum instantaneous lateral force is present on the caudal fin due to the large side area and lateral beating speed. On the caudal fin, the lateral force is high and decreases sharply due to the area decrease along the midline. Prior to the caudal fin, the force on the peduncle is small, and the middle trunk exhibits a relatively large lateral force again. Overall, at most specific times, the head and tail generate lateral forces in the same directions, while the lateral force on the trunk has the opposite direction, which is a characteristic of *carangiform* swimmers.

Compared to hydrodynamic forces, the distribution pattern of inertial forces is significantly different (Fig. 3C and D). In the *x* direction, the inertial force is concentrated at the more forward position (0.31 L), due to the large cross-sectional area. At the same time, although the head has a smaller cross-sectional area, the lateral oscillation of the head during the fluctuating motion is larger than that of the middle position, leading to a concentration of inertial lateral force at the head position.

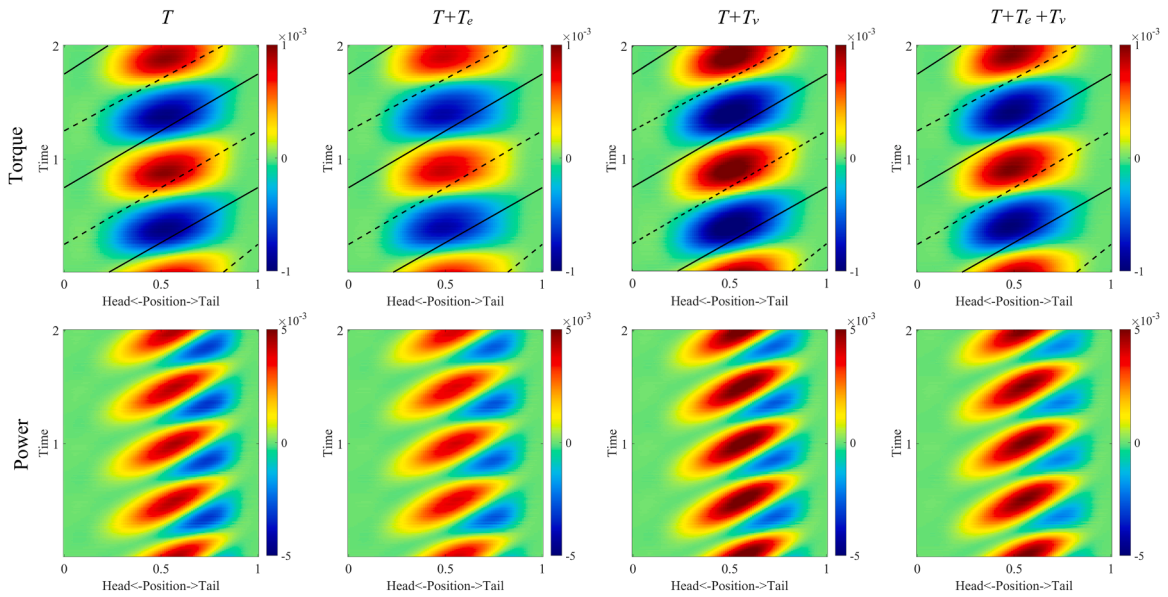

Fig. 14. Distributions of torque (upper row) and power (lower row) when elasticity and viscosity are taken into account.

Table 3
The maximum torque and the speed of the torque wave, when elasticity and viscosity are taken into account.

Models	T	$T+T_e$	$T+T_v$	$T+T_e+T_v$
Max Torque ($\times 10^{-4}$)	9.68	8.37	11.02	10.11
v_T (L/T)	3.31	3.27	3.52	3.53

The internal torques were obtained by including both the inertial and hydrodynamic effects, and the spatiotemporal distributions are shown in Fig. 4A. The large torque value is close to the middle of the trunk, $0.25\text{L} < s < 0.82$ L, defined by 25 % of the maximum value. The maximum torque value is 9.68×10^{-4}, which occurs in the middle of the fish (0.52 L). Meanwhile, the tail and head show little torque. The alternating positive and negative torque values over time refer to the alternating contraction and relaxation of the muscles on both sides of the fish's body. The NPL is also observed in Fig. 4A, as the speed of the torque wave moving backward, ν_{T}, is 3.31 L/T, which is higher than the propagation speed of the body curvature wave $\nu_0 = 1.0$. Ming et al. showed similar results in a mackerel fish model, which shared the same middle line curvature with our model (Fig. 4B) (Ming et al., 2019). In comparison, the speed of the torque wave is 2.11 L/T, which is much lower than that of Carp. Despite that it is mentioned by Ming et al. that the torque wave speed is affected by the body viscoelasticity, the hydrodynamic or inertial effect might cause the wave speed variation.

Regarding the position where torque peaks, the crucian model is anterior to the mackerel fish ($s = 0.52$ L and $s = 0.58$ L, for crucian and mackerel, respectively). At this position, the maximum torques of the two models are similar but in different phases (Fig. 5A). When plotting the torque due to inertial and fluid dynamics separately, we found that the dimensionless inertial torques of these two models are similar, but the hydrodynamic torques are in different phases (Fig. 5C and D). This infers that it is the hydrodynamic effect that causes the phase difference in muscle activation, and thus the value of torque wave speed. Meanwhile, the specific stresses are quite different (Fig. 5B), with $\sigma^* = 56.4$ and $\sigma^* = 43.5$, which might be due to locations of maximum torque, as the carp has a larger arm length of force on the caudal fin.

3.2. *Effects of dorsal and anal fins: kinematics and dynamics*

To study the effects of dorsal and anal fins, we compare the models with either dorsal or anal fins or both. Combined with the model without dorsal and anal fins, four models give different swimming speeds (Fig. 6). Model i reaches the highest average cruising speed $\overline{V_x} = 0.312$, while model ii obtains the lowest $\overline{V_x} = 0.306$, with models with dorsal or anal fin models in between. However, the periodic variation amplitudes are the same for all four models ($\sim$1 %$\overline{V_x}$).

Due to temporal evolution undulation, all fish models experience side shifting in the lateral direction despite symmetric kinematics. In comparison, model iv, with only an anal fin, experiences the least yaw turning, while model iii, with only a dorsal fin, experiences the largest yaw turning. Meanwhile, in between are model i and model ii (Fig. 7).

Four models show the same pattern of the spatioteporal distribution of internal torque but are quantitatively different. In all models, the maximum values, although different, occur at the same location, that is, at 0.52 L. The specific value of 0.96 for model iii maximum torque and the torque wave propagation velocity $\nu_T = 3.33$ are both the largest, while model iv has the smallest maximum

torque of 9.50 and torque wave velocity $\nu_T = 3.07$. The values of the maximum torque and torque wave speed are shown in Fig. 8, and the variation among models is the same as the yaw rotation. The power by muscle actuation is computed as$P_T(s,t) = T\dot{\kappa}$. Fig. 9A shows the distribution of internal power P_T. We can see that the power in the anterior part is almost positive, which indicates the energy output of muscles. However, in the posterior part of the body, near the peduncle position, positive and negative values alternate. A negative power value means that the fish gains energy from the fluid during the undulation. This confirms that energy from swimming was supplied primarily by the mid-body muscle, transmitted through the body in the form of elastic energy(Ming et al., 2019). All four models show the same pattern but with different amplitudes. Fig. 9B shows the time history of the internal power at the positions of 0.51L(the position where the cycle average power is the largest) and 0.76L(the position of the peduncle). The internal power at 0.51 L is ahead of that at 0.76 L in phase and is also large in value.

By integrating the internal power of each segment in time, we can obtain the distribution of the work done by the muscle over a cycle along the body axis (Fig. 10A). The peak positive value is at 0.51 L, while the peak negative value is at 0.81 L (slightly posterior to the peduncle). At 0.51 L, model ii has the smallest power output, and model iii has the highest power output, which indicates that the presence of the anal fin reduces the torque and consequently the power output. Meanwhile, at 0.81 L, model iii has the largest negative power, and model iv has the smallest negative power. As the location difference of the dorsal and anal fins induces a phase difference, such a difference affects energy transmission and recapture (Fig. 10B).

3.3. Efficiency and wake structure

The efficiencies and related parameters of different models are given in Fig. 11A and Table 2. Although both the dorsal and anal fins increase the swimming speed of the fish, the efficiencies defined in both ways of the model i are less than that of the model ii, which contradicts to the observation by Han et al.(Han et al., 2020). Two reasons might cause such a difference. First, the efficiencies in our models refer to swimming at different speeds. The speed of model i is higher than that of model ii, and the low efficiency might be due to the Reynolds number effect. Second, the presence of dorsal and anal fins increases the thrust of the fish while increasing the lateral force, and the low aspect ratio fins are less efficient. For model iv in particular, the increased lateral force results in a larger increase in output power (Fig. 11B), which has a negative impact on efficiency calculations. Please be aware that the differences between the four models are not substantial because the dorsal and anal areas are small in comparison to the overall surface. We enlarge the fin size in the model by 20 % in both the horizontal and vertical directions because these median fins are often small (see Figure S6 and Table S2 in the supplemental materials) and the results reveal the same pattern.

To better understand the mechanisms by which the dorsal and anal fins influence swimming performance, we investigated the evolution of the 3D vortex structure of Model i and model ii. The posterior body vortices (PBVs) of Model i are much more complicated than those of model ii, while the size is also larger (Fig. 12). In model i, the dorsal PBV(DF) is morphologically more elongated, while the anal PBV(AF) is morphologically shorter but thicker, and a larger portion of the PBV is intercepted directly by the caudal fin during the caudal fin swing, which means that the PBV from model i brings more energy to the caudal fin. The different PBVs develop on the caudal fin and then gradually shed from the caudal fin and induce the formation of different morphological leading-edge vortex (LEV). The results of this paper show that the presence of dorsal and anal fins improves the propulsive performance of the caudal fin by altering the morphology of the PBV and inducing a stronger caudal fin LEV, consistent with the findings of the work of Han et al.(Han et al., 2020).

4. Discussions

4.1. Forces on trunk and fins

Fig. 13 shows the force variation on the trunk and three fins of model i. As the dorsal and anal fins are small in size (Table 1), the forces on these two fins are relatively small compared to the forces on the body and caudal fin and generate much less force. However, their phase differences from the trunk and tail affect the torque. Because the arm length of the force in the x direction is small, the lateral force dominates the internal torque. For the *carangiform* pattern, the caudal fin and trunk have an approximately reversal phase on the lateral force. If the phase of the force on the body trunk has a locomotion cycle of 2π, we can see that the phase of the force on the dorsal fin is advanced by 0.08π, while the force on the anal fin lags behind by 0.18π, which can explain why the dorsal fin and anal fin have different effects on yaw turning. Since the dorsal fin increases the propagation speed of torque, while the anal fin decreases the propagation speed, it is inferred that the phase of lateral force changes the propagation speed. However, Han et al. used the real kinematics in which the dorsal/anal fins were in different phases with the trunk, and the forces on the trunk and dorsal/anal fins shared the same phase (Han et al., 2020). This shows that in-phase motion might not be preferred by real fish for muscle actuation reasons.

4.2. Effect of viscoelalticity

In our approach, the total internal torque—the torque brought about by the hydrodynamic and inertial effects—is taken into account, whereas the effects of the trunk's elasticity and viscous damping are ignored. We disregard $T_{elastic}$ and $T_{viscous}$ for two different reasons. 1) According to a research of the sandfish lizard (Ding et al., 2013), the torques caused by these two forces are over an order of magnitude smaller than the maximum torque. A measurement of the stiffness of eels (Long, 1998) likewise revealed a 20 % ratio between unstimulated and stimulated stiffness. Our carp model, in contrast, is more like the sandfish lizard than the thin eels with regarding to the ratio between the body length and the radius of cross section, and the viscoelastic impact is minimal. 2) There is

currently a dearth of trustworthy models for predicting passive viscoelasticity torque. A commonly used model to predict the elastic effect is based on Euler-Bernoulli beam theory (Godoy-Diana and Thiria, 2018; Xu and Yu, 2023). By varying the stiffness of the model, researchers have discovered that a particular stiffness for optimal swimming performance exists. However, the stiffness that maximizes acceleration, steady swimming speed and efficiency might be different (Quinn and Lauder, 2021), and the reliable values of Young's modulus for real fish are still scarce. As the systematical study of the elastic and damping effect is beyond the scope of this paper, we just aim to show briefly how elastic and damping effect might affect the muscular torque, which can be achieved using a simple model by introducing elastic and damping torque on top of the torque in Eq. (8). The elastic and damping torques are assumed to account for 20 % of the actuation torque in our models, then the formula of these torques are as follows,

$$T_e = 0.2\langle T\rangle\kappa(s,\ t)/\langle\kappa\rangle \text{and } T_v\ = 0.2\langle T\rangle\dot{\kappa}(s,\ t)/\langle\dot{\kappa}\rangle \tag{13}$$

Then, when taking into account elastic, damping, and both effects, the actuation torques are $T+\ T_e$, $T+T_v$ and $T\ +T_e\ +T_v$ respectively, and Fig. 14 compares these models. When only elastic effect is taken into account, the actuation torque decreases with a reduction in wave propagation; when just damping effect is taken into account, the actuation torque increases with an increase in wave propagation (Table 3). The opposite effect is produced by the elastic and damping effects. Our thorough research is nevertheless constrained by the dearth of valid data and models. In Figure S7 and Table S3, we also listed the impact of viscoelasiticity with 10 % of the actuation torque, which gives similar results.

4.3. Hydrodynamic roles of the anal and dorsal fins

The dorsal fin can serve passively to generate lateral force, acting as a keel or body stabilizer during cruising swimming (Aleev, 1969; Harris, 1936), as the lateral force on the dorsal fin could induce roll and yaw torque. When studying the kinematics of rainbow trout, Drucker et al. discovered that dorsal fin height and sweep amplitude decrease with increasing speed during steady swimming (Drucker and Lauder, 2005). During fast swimming at a speed of 2.0 body length/s, the dorsal fin is no longer recruited to add momentum to the wake. Meanwhile, the sunfish (Lepomis) used the dorsal fin to generate thrust at higher speed (Drucker and Lauder, 2001). The dorsal fin of trout generates approximately 7.7 % of the thrust generated by the tail at a swimming speed of 1.0 Ls^{-1}. During steady swimming at approximately 1 Ls^{-1}, the sunfish soft dorsal fin contributes 12.1 % of the total thrust force generated by the median and paired fins. In the modeling of a tuna-like model, Zhong et al. found that dorsal/anal fins cause a 15 % increase in speed as well as a 50 % increase in swimming economy (Zhong et al., 2019). The diversity of locomotion in these fishes modulates the roles of the dorsal fin, while the diversity of the morphology of the dorsal fin also affects its hydrodynamic role. For example, the sunfish has a dorsal fin that elongates along the body on the tip, indicating thrust generation orientation. The dorsal fins of bamboo sharks are separated and move laterally independently during steady swimming. The thrust is generated, with the first dorsal fin moving in a larger range laterally than the second dorsal fin (Maia and Wilga, 2013). In addition, Domenici et al. emphasized the role of the rise in the lateral and angular added mass to dorsal fin in reducing lateral oscillation and angular rotations, the erect dorsal fin probably act as control surfaces to increase body stability(Domenici et al., 2014; Paniccia et al., 2021).

For the boxfish of ostraciiform swimmers, the anal fin acts as an important thrust-generating surface, while the dorsal fin is rarely used (Hove et al., 2001). However, for *carangiform* swimmers, using the anal fin only without the movement of the dorsal fin is rare. The anal fin oscillates in the same phase as the dorsal fin during cruising swimming of bluegill sunfish (Standen and Lauder, 2005). The same phase indicates the side force in the same direction, generating the counter rolling torque during cruising swimming. During maneuvers, the fin area is maximized, and the mean lateral excursion of both fins is greater than during steady swimming, with large variation among maneuvers.

Dorsal and anal fins are actuated separately by fish, with the inclinator muscle adjacent to them actuating the motion (Jayne et al., 1996). Although the study of actuation of these two fins is scarce, EMGs show that the actuation of the Bluegill Sunfish dorsal fin is dependent on the red myomeric muscle, although the dorsal fin also shows backward propagation (Jayne et al., 1996). Similarly, the actuation of the anal fin is dependent on the red myometric muscle as well. However, in our model, the force on the dorsal anal fins changes the torque on the body in terms of strength and wave propagation speed. Since the motion of the middle line is specified in our modeling, which is not the case in the real world, the motion might be reshaped by the presence of dorsal and anal fins while keeping the muscle actuation the same.

4.4. Limitations of the study

For the kinematics of real fish, the dorsal and anal fins usually have a phase lag with the body (Drucker and Lauder, 2005; Standen and Lauder, 2005). Such lag causes the wake shed from these two fins to be captured by the caudal fin in different influences. As the oscillation of the fins changes with cruising speed (Standen and Lauder, 2005), we simplify our model and use fins moving in the same manner as the body. Although the phase of the lateral force on the dorsal and anal fins affects internal torque, we analyze the in-phase case as a starting point to study the effects of the dorsal and anal fins on red myomeric muscle actuation. In addition, the Reynolds number in CFD is approximately 4000, which is much smaller than the real fish, and it might cause the final cruising speed to be smaller than the real cruising speed. Fortunately, previous studies on fish swimming indicate that the transition from the viscous regime to the turbulent regime occurs at a *Re* of several thousand (van Weerden et al., 2014), and the model in our study shows an inertia-dominated mode of swimming, making our conclusion qualitatively reliable. The model we utilized in this study ignores the myomeres' conical shape and is homogeneous for the muscle. According to the reference (Alexander, 1969), the strain on the

transection plane for a conical shape is typically uniform on the lateral side, but it may experience opposing strains in the dorsal-ventral direction (Leeuwen, 1999). Although it smooths out the specific information found in the muscles of a real fish, our homogenous model provides the average torque on the transection plane and is useful for guiding the design of soft robotic fish.

5. Conclusion

In this paper, we investigated the swimming performance and muscle activation patterns in fish with and without dorsal and anal fins. Using 3D CFD simulations, we simulated the fish swimming forward and compared the results with mackerel using the same kinematics but with different body shapes. The differences in speed, torque wave speed and muscle stress originate from the geometrical effect. In comparative analyses with and without dorsal and anal fins, dorsal and anal fins enhance swimming thrust and speed of the fish but impair swimming efficiency at its self-propelled final swimming speed. In addition, the dorsal fin increases the internal torque, the speed of the torque wave and the efficiency, while the anal fin decreases them. The adverse effects of these two fins are due to the difference in the phase of the forces generated on them and consequently affect the muscle actuation in the midbody and energy transmission around the peduncle, resulting in varying degrees of NPL. Soft robotic fish mimics the natural movement of actual fish and is distinguished by exceptional energy economy. Fish-like robot fish with adjustable stiffness have been shown to swim quickly and effectively (Zhong et al., 2021). The actuation pattern of soft robotic fish is guided by the torque variation and the resulting swimming performance to attain the ideal stiffness. By far, the majority of soft robot fish don't accurately represent real fish, whose dorsal and anal fins are on the soft actuation (Marchese et al., 2014; Katzschmann et al., 2018). This study clarifies the impact on the actuation of the robot fish and also provides instructions for installing the dorsal/anal fins.

6. Ethical statement

Not applicable.

CRediT authorship contribution statement

Yuhan Li: Methodology, Software, Formal analysis, Investigation, Writing – original draft, Visualization. **Jialei Song:** Conceptualization, Methodology, Formal analysis, Writing – original draft, Writing – review & editing, Supervision, Project administration, Funding acquisition. **Yong Zhong:** Conceptualization, Writing – review & editing, Supervision, Funding acquisition. **Bo Yin:** Software, Resources, Writing – review & editing.

Declaration of Competing Interest

The authors declare that they have no known competing financial interests or personal relationships that could have appeared to influence the work reported in this paper.

Data availability

No data was used for the research described in the article.

Acknowledgment

This work was supported by Guangdong Provincial Key Laboratory of Intelligent Disaster Prevention and Emergency Technologies for Urban Lifeline Engineering (No.2022B1212010016) to YZ and JS, the Guangdong Basic and Applied Basic Research Foundation (No. 2020A1515110584) and the DGUT startup (No. 211135014) grant to JS, the Natural Science Foundation of Guangdong Province (No. 2022A1515011479) and the National Natural Science Foundation of China under Grant (No. 62103152) to YZ.

Supplementary materials

Supplementary material associated with this article can be found, in the online version, at doi:10.1016/j.jfluidstructs.2023.104000.

References

Aleev, I.U., 1969. Function and gross morphology in fish. Smithsonian Libr. Arch. Function and gross morphology in fish.
Alexander, R.McN., 1969. The orientation of muscle fibres in the myomeres of fishes. J. Mar. Biol. Ass. U.K. 49, 263–290.
Altringham, J.D., Ellerby, D.J., 1999. Fish swimming: patterns in muscle function. J. Exp. Biol. 202, 3397–3403.
Borazjani, I., Sotiropoulos, F., 2010. On the role of form and kinematics on the hydrodynamics of self-propelled body/caudal fin swimming. J. Exp. Biol. 213, 89–107.

Chen, J., Friesen, W., Iwasaki, T., 2011. Mechanisms underlying rhythmic locomotion: body–fluid interaction in undulatory swimming. J. Exp. Biol. 214, 561–574.
Ding, Y., Sharpe, S.S., Wiesenfeld, K., Goldman, D.I., 2013. Emergence of the advancing neuromechanical phase in a resistive force dominated medium. Proc. Natl. Acad. Sci. 110, 10123–10128.
Domenici, P., Wilson, A., Kurvers, R., Marras, S., Herbert-Read, J.E., Steffensen, J., Krause, S., Viblanc, P., Couillaud, P., Krause, J., 2014. How sailfish use their bills to capture schooling prey. Proc. R. Soc. B Biol. Sci. 281, 20140444.
Drucker, E.G., Lauder, G.V., 2001. Locomotor function of the dorsal fin in teleost fishes: experimental analysis of wake forces in sunfish. J. Exp. Biol. 204, 2943–2958.
Drucker, E.G., Lauder, G.V., 2005. Locomotor function of the dorsal fin in rainbow trout: kinematic patterns and hydrodynamic forces. J. Exp. Biol. 208, 4479–4494.
Gillis, G.B., 1998. Neuromuscular control of anguilliform locomotion: patterns of red and white muscle activity during swimming in the American eel Anguilla rostrata. J. Exp. Biol. 201, 3245–3256.
Godoy-Diana, R., Thiria, B., 2018. On the diverse roles of fluid dynamic drag in animal swimming and flying. J. R. Soc., Interface 15 (139), 20170715.
Han, P., Lauder, G.V., Dong, H., 2020. Hydrodynamics of median-fin interactions in fish-like locomotion: effects of fin shape and movement. Phys. Fluids 32, 011902.
Harris, J., 1936. The role of the fins in the equilibrium of the swimming fish: I. Wind-tunnel tests on a model of Mustelus canis (Mitchill). J. Exp. Biol. 13, 476–493.
Hess, F., Videler, J., 1984. Fast continuous swimming of saithe (Pollachius virens): a dynamic analysis of bending moments and muscle power. J. Exp. Biol. 109, 229–251.
Hove, J., O'Bryan, L., Gordon, M.S., Webb, P.W., Weihs, D., 2001. Boxfishes (Teleostei: ostraciidae) as a model system for fishes swimming with many fins: kinematics. J. Exp. Biol. 204, 1459–1471.
Jayne, B.C., Lozada, A.F., Lauder, G.V., 1996. Function of the dorsal fin in bluegill sunfish: motor patterns during four distinct locomotor behaviors. J. Morphol. 228, 307–326.
Katzschmann, R.K., DelPreto, J., MacCurdy, R., et al., 2018. Exploration of underwater life with an acoustically controlled soft robotic fish. Science Robotics 3, eaar3449.
Lauder, G.V., Drucker, E.G., 2004. Morphology and experimental hydrodynamics of fish fin control surfaces. IEEE J. Oceanic Eng. 29, 556–571.
Leeuwen, J.L.V., 1999. A mechanical analysis of myomere shape in fish. J. Exp. Biol. 202 (23), 3405–3414.
Lighthill, M.J., 1970. Aquatic animal propulsion of high hydromechanical efficiency. J. Fluid Mech. 44, 265–301.
Long Jr., J.H., 1998. Muscles, elastic energy, and the dynamics of body stiffness in swimming eels. Am. Zool. 38 (4), 771–792.
Maia, A., Wilga, C.A., 2013. Function of dorsal fins in bamboo shark during steady swimming. Zoology 116, 224–231.
Marchese, A.D., Onal, C.D., Rus, D., 2014. Autonomous soft robotic fish capable of escape maneuvers using fluidic elastomer actuators. Soft Robotics 1, 75–87.
McMillen, T., Williams, T., Holmes, P., 2008. Nonlinear muscles, passive viscoelasticity and body taper conspire to create neuromechanical phase lags in anguilliform swimmers. PLoS Comput. Biol. 4, e1000157.
Ming, T., Jin, B., Song, J., Luo, H., Du, R., Ding, Y., 2019. 3D computational models explain muscle activation patterns and energetic functions of internal structures in fish swimming. PLoS Comput. Biol. 15, e1006883.
Paniccia, D., Graziani, G., Lugni, C., Piva, R., 2021. The relevance of recoil and free swimming in aquatic locomotion. J. Fluids Struct. 103, 103290.
Quinn, D., Lauder, G., 2021. Tunable stiffness in fish robotics: mechanisms and advantages. Bioinspir. Biomim. 17 (1), 011002.
Rome, L.C., Swank, D., Corda, D., 1993. How fish power swimming. ScienceScience 261, 340–343.
Sfakiotakis, M., Lane, D.M., Davies, J.B.C., 1999. Review of fish swimming modes for aquatic locomotion. IEEE J. Oceanic Eng. 24, 237–252.
Song, J., Luo, H., Hedrick, T.L., 2014. Three-dimensional flow and lift characteristics of a hovering ruby-throated hummingbird. J. R. Soc., Interface 11, 20140541.
Song, J., Tobalske, B.W., Powers, D.R., Hedrick, T.L., Luo, H., 2016. Three-dimensional simulation for fast forward flight of a calliope hummingbird. R. Soc. Open Sci. 3, 160230.
Song, J., Zhong, Y., Du, R., Yin, L., Ding, Y., 2021. Tail shapes lead to different propulsive mechanisms in the body/caudal fin undulation of fish. Proc. Inst. Mech. Eng. Part C J. Mech. Eng. Sci. 235, 351–364.
Song, J., Zhong, Y., Luo, H., Ding, Y., Du, R., 2018. Hydrodynamics of larval fish quick turning: a computational study. Proc. Inst. Mech. Eng. Part C J. Mech. Eng. Sci. 232, 2515–2523.
Standen, E., Lauder, G.V., 2005. Dorsal and anal fin function in bluegill sunfish Lepomis macrochirus: three-dimensional kinematics during propulsion and maneuvering. J. Exp. Biol. 208, 2753–2763.
Syme, D.A., 2005. Functional properties of skeletal muscle. Fish Physiology 23, 179–240.
Tytell, E.D., Hsu, C.-Y., Williams, T.L., Cohen, A.H., Fauci, L.J., 2010. Interactions between internal forces, body stiffness, and fluid environment in a neuromechanical model of lamprey swimming. Proc. Natl. Acad. Sci. 107, 19832–19837.
Van Leeuwen, J., Lankheet, M., Akster, H., Osse, J., 1990. Function of red axial muscles of carp (Cyprinus carpio): recruitment and normalized power output during swimming in different modes. J. Zool. 220, 123–145.
van Weerden, J.F., Reid, D.A., Hemelrijk, C.K., 2014. A meta-analysis of steady undulatory swimming. Fish fisheries 15, 397–409.
Videler, J.J., 1993. Fish Swimming. Springer Science & Business Media.
Wardle, C., Videler, J., 1993. The timing of the electromyogram in the lateral myotomes of mackerel and saithe at different swimming speeds. J. Fish Biol. 42, 347–359.
Wardle, C., Videler, J., Altringham, J., 1995. Tuning in to fish swimming waves: body form, swimming mode and muscle function. J. Exp. Biol. 198, 1629–1636.
Weihs, D., 1989. Design features and mechanics of axial locomotion in fish. Am. Zool. 29, 151–160.
Williams L., Grillner S., Smoljaninov, V.V., Allen, P., Kashin, S., 1989. Locomotion in lamprey and trout: the relative timing of activation and movement.
Xu, M., Yu, Y., 2023. Effects of body stiffness on propulsion during fish self-propelled swimming. Phys. Fluids 35 (7).
Zha, W., Huang, M., Zeng, Y., 2019. Swimming behavior of crucian carp in an open channel with sudden expansion. River Res. Appl. 35, 1499–1510.
Zhong, Q., Dong, H., Quinn, D.B., 2019. How dorsal fin sharpness affects swimming speed and economy. J. Fluid Mech. 878, 370–385.
Zhong, Y., Wu, J., Wang, C., Li, Y., Song, J., 2022. Hydrodynamic effects of the caudal fin shape of fish in carangiform undulatory swimming. Proc. Inst. Mech. Eng. Part C J. Mech. Eng. Sci., 09544062211069007
Zhong, Q., Zhu, J., Fish, F.E., 2021. Tunable stiffness enables fast and efficient swimming in fish-like robots. Science Robotics 6, eabe4088.